Understanding interfacial fracture behavior between microinterlocked soft layers using physics-based cohesive zone modeling

Navajit S. Baban,[1,2] Ajymurat Orozaliev,[1] Christopher J. Stubbs,[3] and Yong Ak Song[1,4,*]

[1]*Division of Engineering, New York University Abu Dhabi, Abu Dhabi, United Arab Emirates*

[2]*Department of Mechanical and Aerospace Engineering, New York University, New York, New York 11201, USA*

[3]*Department of Mechanical Engineering, University of Idaho, Moscow, Idaho 83848, USA*

[4]*Department of Chemical and Biomolecular Engineering, New York University, New York, New York 11201, USA*

(Received 25 November 2019; revised 9 April 2020; accepted 16 June 2020; published 10 July 2020)

We examine the underlying fracture mechanics of the human skin dermal-epidermal layer's microinterlocks using a physics-based cohesive zone finite-element model. Using microfabrication techniques, we fabricated highly dense arrays of spherical microstructures of radius $\approx 50\,\mu$m without and with undercuts, which occur in an open spherical cavity whose centroid lies below the microstructure surface to create microinterlocks in polydimethylsiloxane layers. From experimental peel tests, we find that the maximum density microinterlocks without and with undercuts enable the respective $\approx$4-fold and $\approx$5-fold increase in adhesion strength as compared to the plain layers. Critical visualization of the single microinterlock fracture from the cohesive zone model reveals a contact interaction-based phenomena where the primary propagating crack is arrested and the secondary crack is initiated in the microinterlocked area. Strain energy energetics confirmed significantly lower strain energy dissipation for the microinterlock with the undercut as compared to its nonundercut counterpart. These phenomena are completely absent in a plain interface fracture where the fracture propagates catastrophically without any arrests. These events confirm the difference in the experimental results corroborated by the Cook-Gordon mechanism. The findings from the cohesive zone simulation provide deeper insights into soft microinterlock fracture mechanics that could prominently help in the rational designing of sutureless skin grafts and electronic skin.

DOI: 10.1103/PhysRevE.102.012801

I. INTRODUCTION

Skin is the largest organ of the human body. It is arranged similar to a brick and mortar configuration at the cellular level, where skin cells resemble brick and skin lipids (oils) resemble mortar [1,2]. This type of architectural arrangement makes the skin highly resilient and compliant: it can withstand high deformations without undergoing catastrophic failure. At the dermal-epidermal junction, the skin uses a strategy of form-based microinterlocking to increase the interlayer mechanical integrity [3,4]. The junction consists of undulating epithelial extensions known as rete ridges that project into the connective tissue-made dermis [5]. These interlocked microridges do many things. They provide firm adherence and mechanical support for the epidermis. They act as a partial barrier against the exchange of cells and large molecules. Perhaps most importantly, they provide effective stress transmission to underlying mechanoreceptors for enhanced tactile sensing [2,3]. When strained, these kinds of periodic features channel nonlinear deformations that help check the corresponding cracks to propagate and thereby significantly increase interfacial fracture toughness [6–10]. This aspect of microinterlocks has been widely exploited to mimic skinlike tactile sensing [3,11–14] as well as to increase fracture toughness among brittle interfaces [15,16], soft-hard interfaces [17], and interfaces involving nanointerlocks [18]. However, so far, no work has been reported concerning soft-soft microinterlocked interfaces devoted to understanding the related microinterlock fracture mechanics. This is most likely due to limited accessibility of these dynamic microscale fracture phenomena for *in situ* microscopic imaging, which is intrinsically challenging and unwieldy to perform at a micrometer scale. Hence, there is a lack of clear understanding of the underlying soft microinterlock fracture mechanics as well as the physics behind the increased fracture toughness of soft microinterlocked layers. To understand the fracture mechanics and critically assess the role of contact interaction in determining interfacial fracture toughness, the situation demands clear visualization and energetics of crack propagation via a single microinterlock.

In this study, we report a physics-based simulation approach to understand the role of microinterlocks in soft interfacial fracture by visualizing the contact interaction and quantifying the related energetics during the fracture at a single microinterlock level. A cohesive zone finite-element model (FEM) simulation was performed using Abaqus®/CAE 2016 Standard where all the required parameters were obtained via experiments to maintain the physical conditions as closely as possible, hence the name physics-based model. Using the model, we measured elastodynamic energetics of crack propagation via a single microinterlock fracture and compared the associated strain energy dissipation for different interlock topology. The output showed contact interaction-based phenomena where the primary propagating crack was arrested and the secondary crack was initiated in the microinterlocked

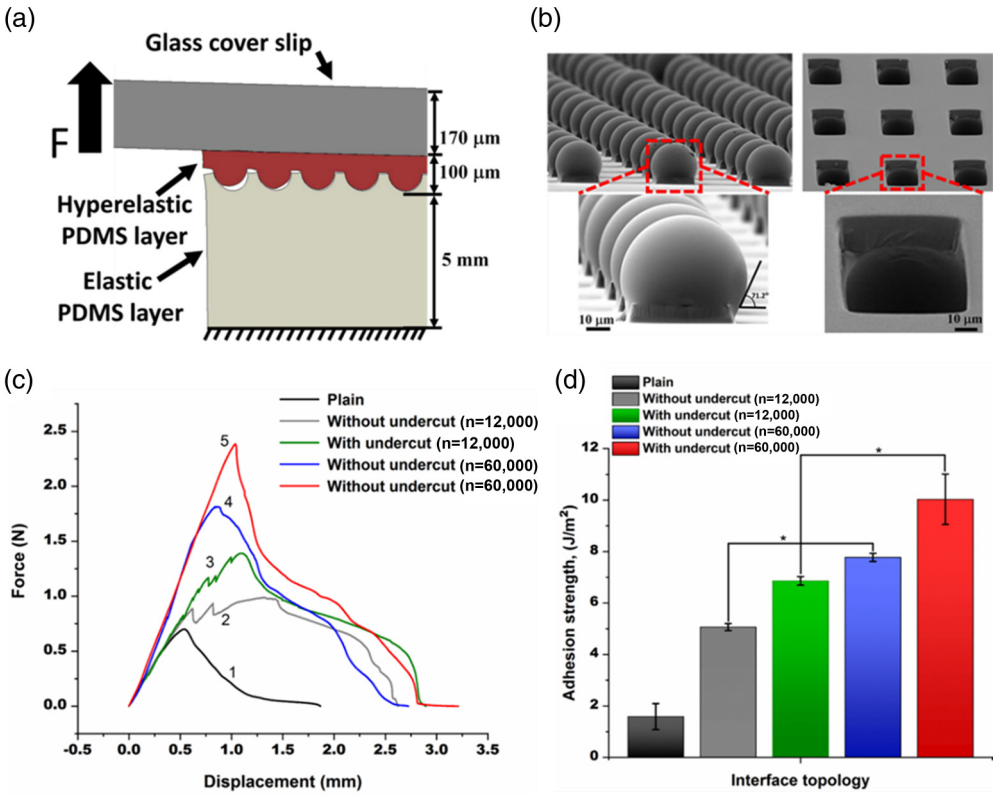

FIG. 1. Bioinspired microinterlocks and single-leg cantilever bend peel test results. (a) Schematic showing 2D view of single-leg cantilever bend test. A plasma-bonded glass coverslip (170 μm) was used as a flexible backing to peel the hyperelastic PDMS layer (100 μm thick) containing spherical microbumps. The hyperelastic PDMS layer was peeled from 5-mm-thick PDMS, which was bottom fixed in all degrees of freedom. The PDMS interface was first plasma treated and then silanized with trichlorosilane to create a predefined fracture region. The components shown are not in proportion. (b) Postpeel SEM micrographs showed a clean interfacial fracture between the spherical microbumps with undercuts and the related complementary spherical microgrooves. The undercut occurs in an open spherical cavity whose centroid lies below the spherical microstructure's surface. The undercut angle, which is the angle swept between the drawn tangent to the spherical surface and the horizontal pedestal surface, was recorded to be $\approx 70^{\circ}$. It is worth note here that both complementary features remained undistorted postfracture even though they had to undergo significant elastic distortion in order to be pulled out through a circular opening having a radius smaller than their spherical radius. (c) Force versus displacement results for five different interface topologies: 1, plain; 2, hemispherical microinterlock without undercut with $n = 12\,000$; 3, hemispherical microinterlock with undercut with $n = 12\,000$; 4, hemispherical microinterlock without undercut with $n = 60\,000$; 5, hemispherical microinterlock with undercut with $n = 60\,000$. The microinterlocks were distributed on the rectangular patch area of 300 mm^2. (d) Adhesion strength (energy required to peel unit surface) values for different interface topologies (sample size, $N = 5$); the error bars represent standard deviation. Significant increase in the adhesion strength was observed for the microinterlocked interfaces ($\approx$2.5-fold without undercut and $\approx$3.5-fold with undercut for $n = 12\,000$) and ($\approx$4-fold without undercut and $\approx$5-fold with undercut for $n = 60\,000$) compared to the plain interface. Also, a significant (P value of 0.01) increase in adhesion strength was observed for the microinterlocks with and without undercut between $n = 12\,000$ and 60000.

area. Between these events, the energy remained stored in the system that would have otherwise be dissipated irreversibly via crack tips, had it not been arrested. These phenomena were completely absent in the plain interface fracture where the fracture propagated catastrophically without any arrests. Strain energy analysis confirmed the significantly different strain energy dissipation rate among different microinterlock topology. The following sections describe in detail the design of the microinterlock and experimental results as well as the physics-based cohesive zone model.

II. DESIGN OF SOFT MICROINTERLOCKS

We fabricated fracture test samples containing the soft microinterlocked interface using polydimethylsiloxane (PDMS). PDMS was chosen because of its propensity towards large interfacial slippage that keeps shear stresses near the delamination front during fracture [19]. To incorporate gradient stiffness similar to a dermal-epidermal layer of skin [20], the layer containing the spherical microbumps (upper layer) was kept thin ($\approx$100 μm) while the layer containing related complementary spherical microgrooves (bottom layer) was kept thick ($\approx$5 mm), as seen in Fig. 1(a). The length and breadth of the sample's patch area were 15 mm and 20 mm, respectively. To obtain a clean interfacial separation, the bottom layer was surface-treated using trichloro (1H, 1H, 2H, 2H-perfluoro-octyl) silane before pouring and spin coating PDMS. The fracture samples were prepared using a spin coating (750 rpm for 2 min) and subsequent curing, which was plasma bonded to a glass coverslip (170 μm thick) as a

backing layer with an overhang of 5 mm. More details about the fabrication and preparation of the sample can be found in Appendix A.

III. EXPERIMENTAL

A. Fracture setup and postfracture microscopy

A displacement-controlled (displacement rate of 5 μm/s) single-bend cantilever fracture peel test setup was designed, which was connected to a load cell (50 N) on an Instron® universal testing machine. The experimental setup is shown in Fig. 8(b) in Appendix A. An extra 4 mm space was added to the edge of the microinterlocked patch area for the peeling experiments, and a precrack in the interface was introduced by manually prepeeling or unbonding the interface starting from the cut edge until reaching the boundary of the microinterlocked area. Once the precrack line met with the start-edge line of the microinterlocked patch area, the peeling layer was then released to let it go back to its initial position. Finally, the sample was mounted and fixed on the Instron machine's base adapter for the start of the peel test. Postfracture scanning electron microscopy (SEM) revealed clean separation of the interface as seen in Fig. 1(b) where no signs of cohesive fracture were observed. This noncohesive fracture was due to the inert monolayer of the silane that was deposited on the bottom PDMS layer before casting, spin coating, and curing of the top PDMS layer, as schematically depicted in Fig. 8(a). The silanization step ensured that there was no permanent bonding between the bottom and the top PDMS layers after curing and allowed for pure adhesive fracture via inducing a predefined fracture propagation path.

B. Interfacial bond nature and characteristic stress decay length

For fracture peel tests, the peel area consisted of $15\times20\,\text{mm}^2$ where five interface topologies were chosen: plain, hemispherical microinterlock without undercut ($n =\approx$ 12 000 and ≈60 000), and hemispherical microinterlock with the undercut ($n =\approx$ 12 000 and ≈60 000). The patterns were arranged in square arrays where the distance between each cell was kept at 120 μm and 30 μm for $n = 12\,000$ and 60000 microbumps, respectively. As per the experimental peel test results, the force responses showed a linear increase till damage initiation followed by postfracture damage evolution that could be approximated using a linear predamage and exponential postdamage traction separation law. As seen in Fig. 1(c), postdamage evolution was rapid and exponential with no steady-state regime or plateau as seen in the works reported by Majumder *et al.* [21]. To find the reason behind this response, we conducted an experiment keeping in view the finite-size effect (lengthwise) and the difference between the interfacial bond nature as compared with Ref. [21]. For the finite-size effect, we performed our peel experiments with three times the peel length, and for the bond-nature effect, we did the same, but this time it was glass coverslip peeled against the plain PDMS (silanized). The results, as seen in Fig. 2, indicated that the rapid postdamage decay reported here in which the interface was PDMS-PDMS (silanized) is

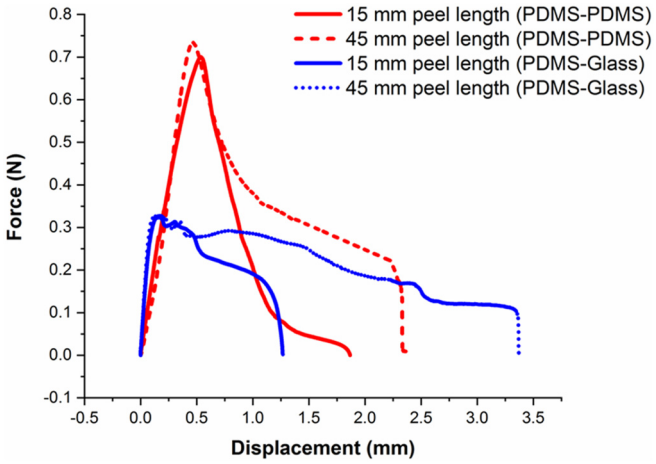

FIG. 2. Force-displacement response as a function of peel length and bond nature. Rapid decay was observed in the case of PDMS-PDMS 15 mm peel length sample as compared to 45 mm peel length, which attained a quasi-steady-state plateau before dropping down to zero as a result of extra length. However, significant plateau length with lower damage initiation force was observed for PDMS-glass 45 mm peel length sample as compared to the 15 mm peel length sample, which signifies that the nature of the bond plays a significant role in crack propagation behavior as well. Hence, peel length and interfacial bond nature play determining a role in crack propagation behavior. The number of samples used here was five for each case.

combined due to the finite size as well as the nature of the interfacial bond.

To explain the characteristics of the curves and higher adhesion strength in the case of the microinterlocked layers, we experimentally evaluated and compared the characteristic stress decay length (k^{-1}) with the spacing between the microinterlocks. The previous studies by Chaudhari *et al.* [22], Ghatak *et al.* [8], Chung *et al.* [23], and Majumder *et al.* [21] calculated the characteristic stress decay length, $k^{-1} = (\frac{Dh^3}{12\mu})^{1/6}$ when peeling off a flexible silanized glass coverslip plate from a PDMS sheet film to quantify the relative deformability-based stress confinement between the film and the plate in the effective contact zone as a function of the confined thin film's thickness (h) and shear modulus (μ) as well as flexural rigidity (D) of the plate. They reported an absence of the crack-arresting effect when the horizontal spacing of the patterns was kept greater than k^{-1}, whereas a significant increase of the same was observed when the spacing was kept considerably less than k^{-1}. When we evaluated the characteristic stress decay length (k^{-1}) for our system, the characteristic stress decay length scale was found to be ≈383 μm as detailed in Appendix B.

The horizontal spacing between the microinterlocks we used ranged from 30 μm to 120 μm, which was significantly less than our system's characteristic stress decay length of $k^{-1} = 383\,\mu$m. The above-mentioned studies reported that the fracture toughness significantly increased when the spacing between the patterns and discontinuities were kept considerably below the characteristic stress decay length. In agreement with their findings, our results also showed that these highly dense microinterlocks significantly contributed to the

increase of adhesion strength during peeling. Also, because of the significantly lower spacing compared to the characteristic stress decay length, the characteristic feature of the individual pattern or discontinuity became inapprehensible in the obtained force-displacement responses.

C. Experimental results and Cook-Gordon mechanism

As per the force-displacement data obtained from the peeling tests, the force required to peel off the microinterlocked layer without and with undercut for $n = 12\,000$ showed a significant increase in the damage initiation force from 0.70 N (plain) to 0.98 N and 1.39 N, respectively, as shown in Fig. 1(c). When the number of microstructures was increased to 60000, significantly higher damage initiation force was recorded as compared to their $n = 12\,000$ counterparts with the values of 1.81 N and 2.38 N, without and with the undercut, respectively. However, the slope of the predamage initiation curve remained surprisingly comparable (1.43 N/mm) for plain layers and $n = 12\,000$ layers, but significantly increased by 63% to 2.33 N/mm for $n = 60\,000$. Similar results were found by Chung *et al.* [23], where they attributed the enhancement of fracture toughness of their crosswise incised PDMS-glass (silanized) interface to the Cook-Gordon (C-G) mechanism [24,25]. According to this mechanism, when a crack propagates on an anisotropic and nonhomogeneous interface with potential cleavage planes, a secondary crack is initiated on the cleavage plane ahead of the primary propagating crack, which then halts and deflects the primary crack, thus decreasing the crack sensitivity and increasing the toughness of the material. While their experiment was conducted in two-dimensional (2D) conditions, in which both the propagation and deflection of crack occurred at the plane interface, our interface consisted of the three-dimensional (3D) form-based microinterlocks. Nevertheless, in our system also the C-G mechanism could be valid during fracture as a result of the induced 3D geometry-based anisotropy or nonhomogeneity and contact-based nonlinearity. To verify this we performed the following experiments.

Adapted from the experiments on transverse incisions from Ref. [23], we fabricated microinterlocked plane strain patterns with the same spacing distance of 120 μm and 30 μm (both for $n = 12\,000$ and 60 000, respectively) to get rid of crack-arresting effect in the transverse direction during the peel test. As per the results shown in Fig. 3, the damage initiation forces in the case of the microinterlocks with 30 μm spacing or $n = 60\,000$ and with 120 μm spacing or $n = 12\,000$ were 1.82 N and 0.67 N, respectively, while their corresponding plane strain patterns showed a damage initiation force of 0.81 N and 0.42 N, respectively. In both cases, there was a significant difference in the damage initiation force between the microinterlocks and the plane strain patterns by 1.5- to 2-fold while their predamage slopes remained comparable at the same spacing. The predamage slope significantly decreased when the spacing increased to 120 μm. These results suggested the prevalence of the C-G mechanism in guiding the fracture response, because unlike the microbump patterns, the plane strain patterns showed no crack arrests in the transverse direction in the predamage phase of peeling.

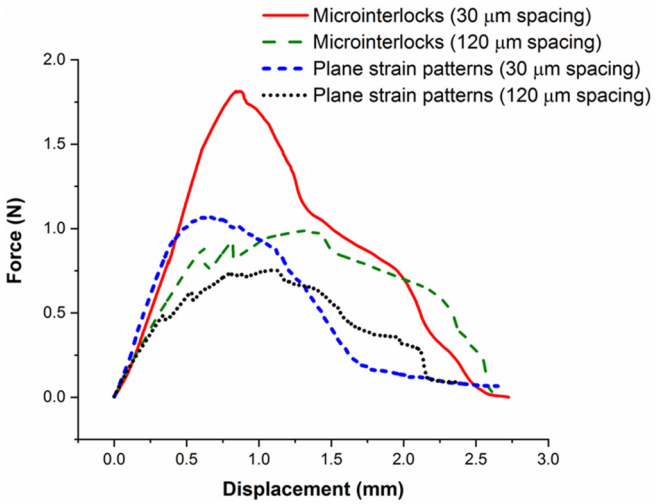

FIG. 3. Force-displacement response for microinterlocked array and plane strain patterns for $n = 12\,000$ (120 μm spacing) and $n = 60\,000$ (30 μm spacing). The predamage slope for the related pairs remained unremarkably the same; however, the damage initiation or crack initiation force significantly differs among the related pairs.

D. Adhesion strength comparison

The adhesion strength of the interface was calculated by integrating the global area under the measured force-displacement response curve, which was subsequently divided by the relevant contact area to obtain the amount of energy needed to mechanically peel per unit area as reported in Refs. [21,26]. As per the adhesion strength results, the use of the highly dense micromechanical interlocks ($n = 12\,000$) without and with undercuts enabled increased adhesion strength between two PDMS layers significantly by $\approx$2.5 and $\approx$3.5, whereas it went as high as $\approx$4 and $\approx$5-fold, respectively, for $n = 60\,000$ as shown in Fig. 1(d). Based on the findings of several studies conducted on biomimetically patterned interfaces [7,8,28] or periodically interlocked hard interfaces [27–29], the reason behind the increase in adhesion strength for a predefined path could be a subtle combination of any of the following phenomena: crack kinking or the C-G mechanism (which we hypothesized as well), equilibrium which hindered the crack's propagation [30–32], architecture-based channeling of the propagating cracks [33–35], and form-based contact mechanics-induced vicinal dissipation [15–17]. Hence, to critically visualize fracture propagation at the single microinterlock level to find the accurate determining fracture mechanism and to gain insights into the governing energy-dissipating mechanism, we developed a physics-based cohesive zone model whose details are given below.

IV. PHYSICS-BASED COHESIVE ZONE MODEL

We made a FEM using the commercial finite element package Abaqus®/CAE Standard where we modeled the soft interfacial layers with 2D idealization. ABAQUS Standard was used because of the chosen slow or quasistatic nature of the peeling process (as the displacement rate used for peeling was 5 μm/s). The parts that were modeled were 5-mm-thick elastic

PDMS, 100 μm hyperelastic PDMS layers, and 170-μm-thick glass coverslip. The boundary conditions were translated from the experimental peel tests where the glass cover slip's relevant surface was tied with the hyperelastic PDMS's surface and the elastic PDMS's bottom edge was constrained in all degrees of freedom (encastre boundary condition). A rigid discrete nondeformable grid part of length 4 mm was used as a deflector for peeling the glass coverslip via contact interaction to replicate the exact physical conditions of the experimental peel test.

Relevant displacement boundary condition was given to the discrete grid deflector based on the experimental data. Nonlinear geometry was kept on during the peeling. The increment initial size of 1E-007, the minimum size of 1E-015, and the maximum size of 1 were used with the maximum number of increments of 5000. Full Newton direct solver was used with linear extrapolation and default matrix storage for the static, general step 1. The reaction force while peeling was extracted by a kinematically coupled reference point to the rigid discrete grid deflector's length. The outcome of the reaction force depended on the bending of the glass coverslip backing layer, which in turn solely depended upon the adherence between the elastic PDMS and hyperelastic PDMS layers. Therefore, the main region of interest of the model was the interfacial contact. The following discussion addresses the cohesive zone modeling of the contact pairs where the zone underwent pure adhesive failure.

The adhesive behavior of the contact pairs was modeled using a zero thickness cohesive surface method [36] where the constitutive interfacial response was designed in the surface-based interaction property manager using the following parameters: cohesive behavior (for prefracture or predamage penalty stiffness), tangential (frictionless or with friction), normal behavior ("hard pressure" overclosure), damage (for fracture response), and geometric properties (for out-of-the-plane thickness of the interface). For the contact interaction, the surface-to-surface discretization method with small sliding was used. Contact controls and automatic stabilization using the interaction manager and step module were used for the solution convergence. The slave surface was adjusted only to remove overclosure, and the initial clearance was kept 0. The surfaces were automatically smoothed wherever it was applicable, and contact controls were given with an automatic stabilization factor of 1. The cohesive zone parameters included cohesive penalty stiffness and damage initiation and propagation parameters. The former decided the predamage response of the interface during deformation, while the latter decided the fracture initiation and propagation behavior. Apart from the above-mentioned parameters, tangential behavior with friction coefficient 1.63 as per Ref. [37] and "hard" contact pressure-overclosure normal behavior were also used to model the contact mechanics with friction. The out-of-plane thickness was modified using geometric properties in the interaction property manager for plane strain interfaces as per the experimental dimensions of the plain interface.

The aforementioned cohesive parameters were determined using the traction separation law [38,39], which is essential to describe the constitutive response of the interface during fracture. This is different from the force-displacement response, which is normally obtained from the usual mechanical load-displacement cell fracture setup [40]. A double or single cantilever beam planar interface fracture specimen can be used in mode I to obtain the traction separation law [38,40]. However, obtaining the traction separation law for a 3D form-based interface, as for our microinterlocked interface, experimentally remains challenging due to the simultaneous engagement of contact mechanics and cohesive or adhesive fracture factors that bring severe nonlinearity in the system [16]. Therefore, to understand the interface fracture using a cohesive zone model while remaining as close possible to the real physical situation, we started with the plain interface modeling with the help of experimentally obtained force-displacement response. We used the FEM as a forward solver to model the constitutive response of the plain interface to obtain the traction separation law via curve fitting the simulation force-displacement curve with the experimental one. To model the material and adhesive behavior of the interacting parts with most appropriate material and cohesive parameters that can capture the physical conditions of the experimental peel test, we performed a series of experiments whose details are given below.

To achieve physics-based cohesive zone modeling of the interfacial fracture behavior, we need information on geometry, material characteristics, boundary conditions, and traction separation behavior. The geometry was determined using microfabrication and SEM analysis. The material characteristic was determined using experimentally determined elastic as well as Ogden fit hyperelastic models (see Appendix C). The boundary conditions were extracted from the experimental peel tests. Decisions about the damage initiation, propagation, and mode-mixity criteria were made using custom-made normal-only and shear-only fracture tests (see Appendix D). Due to the highly nonlinear nature of the microinterlocked interface as a result of geometry, material, and contact-based nonlinearities and associated difficulties related to the convergence of these kinds of FEMs [38,41–43], a plain interface peel test was first simulated to obtain traction separation parameters. The obtained damage criterion parameters from Fig. 13 in Appendix D were used as the initial guess to curve fit the simulation force-displacement response with the experimental one. For damage evolution, exponential softening was used keeping in view the post-damage experimental results. Due to the interlocked nature of the interface combined with the loading conditions, mode mixity was inevitable [18]. Therefore to take care of mode mixity during damage propagation, the Benzeggah-Kenane (BK) form [44] was used where the relative proportion of energy dissipation during fracture propagation in normal and shear directions was considered to determine the required quantitative values for modeling. For this, the area under the curve postdamage initiation was taken from the damage propagation portion of the curves shown in Fig. 13. The areas under the curve for normal (0.00024 N/mm) and shear in two directions (0.235 N/mm, which is three orders higher than the normal direction one) were inserted in the interaction property module for damage evolution. After inserting all relevant parameters representative of experimental physical conditions, the job was run, and results were obtained from the output files for visualization and comparison.

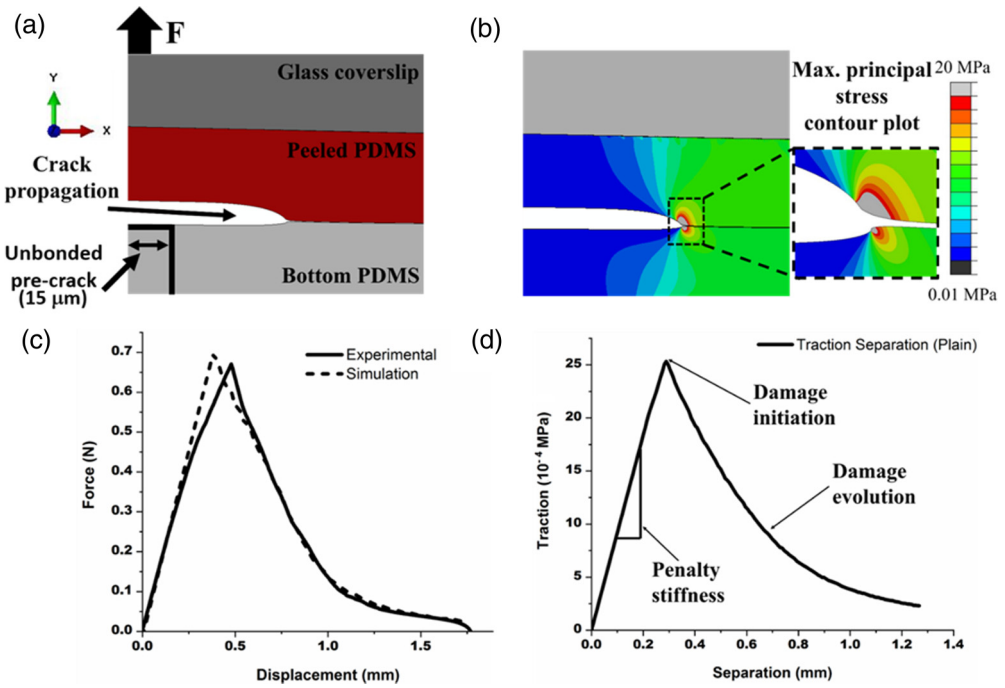

FIG. 4. Extraction of the traction separation parameters to model the interfacial fracture via curve fitting experimental and simulation peel test response. (a) Schematic showing 2D plain approximation of the peel test indicating the involved components with a precrack of 15 μm. (b) Results of the simulation showing the contour plot of maximum principal stress where dissipation at the crack tip was visible. (c) Curve-fitted experimental and simulation force versus displacement curve. The slight variation in the peak region was due to the stress relaxation (viscoelastic) behavior of PDMS during the experimental condition, which was not considered in this simulation. (d) Traction separation behavior of plain interface was extracted via tracking the precrack separating nodes' displacements. The obtained traction separation parameters, namely, penalty stiffness (0.025 N/mm^3), damage initiation (0.0075 N/mm^2), and damage evolution (0.00024 N/mm), were estimated and used to further model the microinterlocked interface.

A. Plain interface traction separation

Using the obtained necessary damage parameters, material characteristics, boundary conditions, and geometry, a 2D plain peel test simulation was performed using plane strain four-node bilinear plane strain and plane stress quadrilateral elements for the bottom elastic PDMS and the top hyperelastic PDMS layer, respectively. As per the experimental sample, the length and out-of-plane thickness were chosen as 15 mm and 20 mm, respectively. To choose the mesh size for the model, a mesh convergence study was conducted, in which simulations were performed after adjusting all the edge seed sizes of each part of the assembly and recording force-displacement responses till the optimum mesh size was decided. The optimum mesh size was determined to be 0.025 mm per element side, as shown in Fig. 14 in Appendix E. More details about the convergence study can be found in Appendix E.

Keeping in view the experimental arrangements made for the precrack (already discussed in Appendix A), an unbonded precrack of 15 μm was given behind the starting point of the cohesive zone, as seen in Fig. 4(a). The redundant and already debonded 3.985 mm length out of 4 mm was not considered for the simulation because our focus remained on to modeling the bonded cohesive zone. Since maximum nominal stress was chosen over maximum separation for the damage initiation criteria, therefore maximum principal stress was considered for analysis. The simulation's output recorded the putative crack tip's stress dissipation during fracture propagation, as seen in Fig. 4(b). The concerned fracture parameters were optimized to curve fit the simulation force-displacement behavior with the experimental one. A close fit between the experimental and simulation curve was obtained, as seen in Fig. 4(c).

Once the force-displacement behavior was modeled, the traction separation behavior was extracted by tracking the precrack separating nodes' displacement during fracture. The traction separation parameters (penalty stiffness = 0.025 N/mm^3, damage initiation = 0.0075 MPa, damage evolution = 0.00024 N/mm) were obtained from the curve shown in Fig. 4(d). The calculated area under the traction separation curve showed that the fracture toughness differed from the thermodynamic work of adhesion by an order of 10^3. The thermodynamic work of adhesion was obtained by a contact angle experiment, as shown in Fig. 5. Thus, interfacial elastic contact interaction and rheological bulk deformation of PDMS highly affected the fracture toughness as compared to chemical-based molecular adhesion, which was measured by the thermodynamic work of adhesion [45,46]. This highlights the mechanical benefits of using rational microinterlock designs that can highly amplify the degree of fracture toughness.

B. Microinterlock fracture

To model the microinterlocked interface fracture, the only topology of the interface was changed according to the

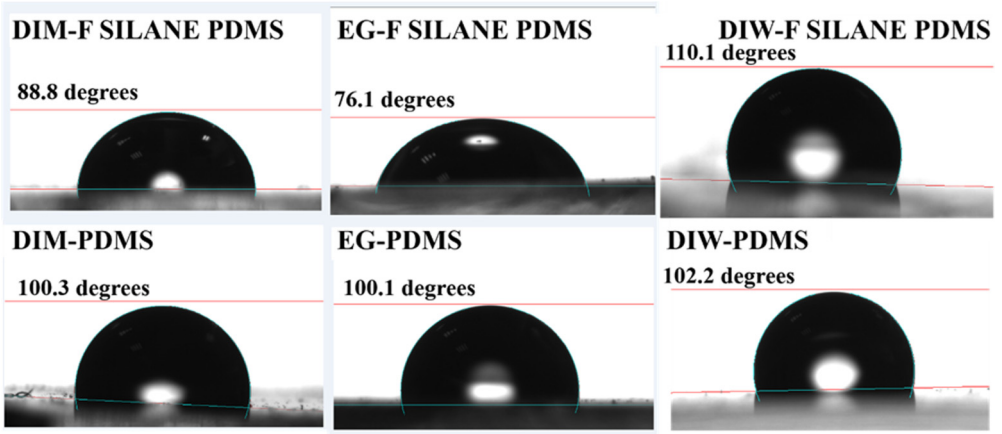

FIG. 5. Theoretical or thermodynamic work of adhesion between PDMS and PDMS (silanized) surfaces using diiodomethane (DIM), ethylene glycol (EG), and distilled water (DIW). The thermodynamic work of adhesion between PDMS-PDMS (silanized) surfaces was found to be 30.65 mJ/m^2, which was less by an order of 10^3 as compared to the experimentally obtained results. The difference could be attributed to the role of contact-based fracture mechanics and rheology of the PDMS layers.

experimental geometry obtained via the SEM micrographs; and keeping all the other inserted parameters the same, the simulation was again run with the contact mesh seed size of 0.0005 mm per element side on the contact interface to keep the interfacial region finely meshed for an accurate solution [16]. The related mesh convergence study is shown in Fig. 15 in Appendix E. When executed, the model ran stably at the beginning of the step; however, due to instabilities developed as a result of the highly nonlinear nature of the problem, the contact-associated field equations did not converge towards the solution. Consequently, the fracture did not propagate as a result of a nonfavorable crack equilibrium [16,41–43]. As we aimed to visualize and find how microinterlock-based contact interaction modified the crack propagation behavior, attaining a stable convergence or fracture propagation was indispensable. To enable the fracture propagation a damping factor of 0.0002 was introduced based on the dissipated energy fraction in the step module for automatic stabilization [36]. Apart from this, a viscous coefficient of 0.0001 was used as the stabilization factor for the contact damage properties as discussed in Refs. [42,43]. Consequently, a stable convergence during the course of the step was achieved and full fracture propagation was attained. The efficacy of using this strategy regarding obtaining accurate solution was evaluated by calculating the dissipation percentage, which was calculated by comparing total strain energy with the sum of all viscous damping and stabilization energies, which came out to be less than 1%. The dissipation percentage was sufficiently small and hence provided an accurate solution.

C. Submodeling and boundary conditions around single microinterlock

The microinterlocked model peeled fully, and the problems associated with nonlinearity and convergence issues were resolved using contact controls and automatic stabilization. However, we wanted to visualize crack propagation through a single microinterlock fracture that differed significantly in terms of the length scale from the full microinterlocked interface model. As a result of this, the selective fine meshing of the region of interest resulted in mesh compatibility problems with nonrelevant regions. Alternatively, when the whole parts meshed, the computational time increased exorbitantly. Therefore, to solve the problem and specifically concentrate on the single microinterlock fracture, we chose the technique of submodeling [36], with the help of which we isolated the region of interest and ran a submodel using the output files from the model out of which the region had been isolated (known as a global model). We successfully executed the running of our submodel via carefully partitioning and translating boundary conditions from the global model as described in Appendix F. As the submodel was a whole FEM in itself, therefore for a given time step, it was possible to extract work done on the system as well as strain energy absorbed by the system in the form of a single whole model output from field history output variables. The obtained numerical values via this approach allowed us for a comparison between undercut versus nonundercut energy dissipation.

V. SIMULATION RESULTS AND DISCUSSION

A. Primary crack arrest and secondary crack initiation

Our FEM accurately captured the phenomenon of contact interaction-induced primary crack arrest and secondary crack initiation at the single microinterlock level. Maximum principal stress was chosen for the contour plots keeping in view high fracture vulnerability towards normal stress compared to shear stress. The contour plots at different time steps for the nonundercut microinterlock captured the counterintuitive series of events, which comprised a contact interaction-based primary propagating crack arrest followed by a secondary crack initiation that ultimately propagated with two crack fronts, as seen in Fig. 6(a). The events can be seen in Supplemental movie 1 in the Supplemental Material [47]. With the same total time step of the simulation, similar events were recorded for the microinterlock with the undercut, as seen in Fig. 6(b), but at delayed time points as due to the undercut (see Supplemental movie 2 [47]).

The microinterlocks introduced geometric nonlinearity as compared to a plain interface due to which simultaneous

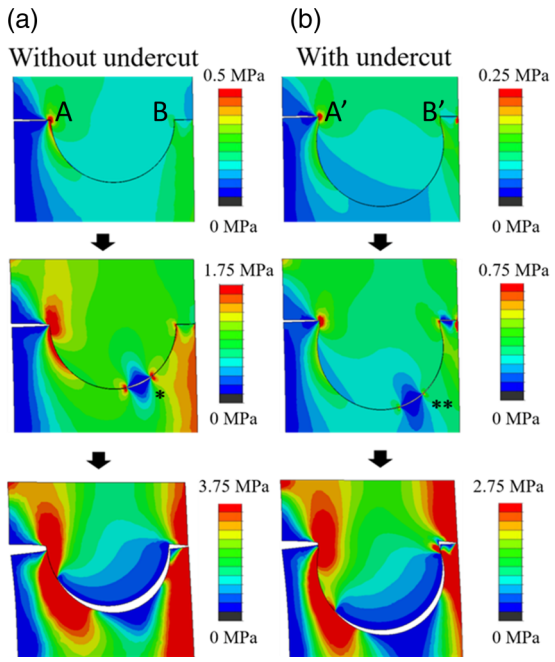

FIG. 6. Primary crack arrest and the secondary crack initiation as a result of contact interaction for a single microinterlock fracture with and without undercut. (a) Maximum principal stress contour plots depicting fracture propagation in the microinterlocked region without undercut. Point markers A and B depict location of start and end points of the nonundercut microinterlock. The primary propagating crack was arrested due to the vicinal microinterlock-based compressive interaction. The secondary crack was initiated with two crack fronts in the adjacent region of the ongoing compressive sliding zone. The single asterisk marks the location of this event. The secondary initiated crack propagated on both sides with two crack tips. (b) Maximum principal stress plots depicting fracture propagation in the microinterlocked region with the undercut. Point markers A′ and B′ depict the location of start and end points of the microinterlock with undercut. The double asterisks mark the location of the secondary crack initiation event for the undercut microinterlock.

compressive and tensile contact interactions took place in the microinterlocked region during deformations. The compressive interaction near the primary propagating crack area closed the crack opening and hence arrested primary crack, while the corresponding vicinal region around the compressive zone became consequently a tensile zone as a result of mode mixity and Poisson's effect and, hence, led to the secondary crack initiation. The curved nature of the interface geometry induced in-plane and out-of-plane distortions due to contact-based interactions leading to a complex state of stress within the interlocked areas generating local variations in a state of stress and the related strain energy release rate inducing complex nonlinearities in energy balance equations. Ultimately, the underlying primary crack arrest and secondary crack initiation phenomenon in the interlocked interface led the fracture propagation into an unstable equilibrium that was different from the plain interface, where the crack initially was transient and then progressed in stable equilibrium staying on the same plane to the end of the bond line similar to the movement of an elastic string on a plane frictionless surface [40,48]. When these events were quantified by plotting the damage criterion and maximum principal stress as a function of true distance along the microinterlock path (with and without undercut) at relevant time steps, as seen in Figs. 7(a)–7(d), the extent of fracture initiation and propagation along the path became evident. When the amount of contact opening was compared for both cases at the same time step of 0.5 s, a significantly lower contact opening was observed for the interlock with an undercut as compared to its nonundercut counterpart due to the interlocking effect, as shown in Fig. 17 in Appendix G.

The damage criterion plotted with a horizontal line at ordinate 0 indicating no fracture and fracture at 1 revealed the region in the microinterlock that was fully damaged. In contrast, the maximum principal stress plot showed conformal behavior with the damage criterion plot as the stress recorded zero value in the damaged region. This conformity was missing in other stress plots like those of von Mises and Tresca that considered shear stresses as well. Thus, the maximum principal tensile stress determined the secondary fracture, or in other words, the crack initiation process was highly guided by the tensile interaction as compressive interaction did not contribute towards contact opening in general. Also, after the secondary crack initiation, the effect of secondary crack propagation was compared between the two cases. It became apparent that due to the undercut, the damage propagation was considerably less as compared to the nonundercut counterpart. It should be noted here that the primary crack remained halted while the secondary crack propagated towards the primary crack till both merged.

To find the effect of the scale and density of the microinterlocks on the contact opening, we performed a simulation on the smaller microinterlocks of radius $\approx 5\,\mu$m with the interspacing distance of 2 μm and 30 μm between the bumps for the same cohesive line distance (115 μm) of a single microinterlock of radius 50 μm, as seen in Fig. 18 in Appendix H. The results suggested that having highly dense smaller microinterlocks (5 μm in radius) can produce similar effects in terms of contact opening as compared to one single big microinterlock (50 μm in radius). However, the widely spaced 5 μm interlocks showed a significant increase in contact opening as compared to the other two microinterlocks. Therefore based on the simulation results, smaller and denser microinterlocks can alter the surface fracture properties significantly via controlling the contact opening through a microinterlocking strategy. This aspect can be utilized in tribology where surface modification is the prime concern with the highest concern is given to decrease the penetration depth of the surface features into the bulk.

B. Energy comparison

As several previous studies have already reported, the crack initiation requires larger energy than crack propagation [8,21,49], and so we chose the event of primary crack arrest and secondary crack initiation for energy dissipation comparison. Figures 8(a) and 8(b) show strain energy density as a function of the true distance along the microinterlock path at the two consecutive events. According to the simulation-based strain energy density analysis, the microinterlock's contact mechanics-based interactions significantly changed the

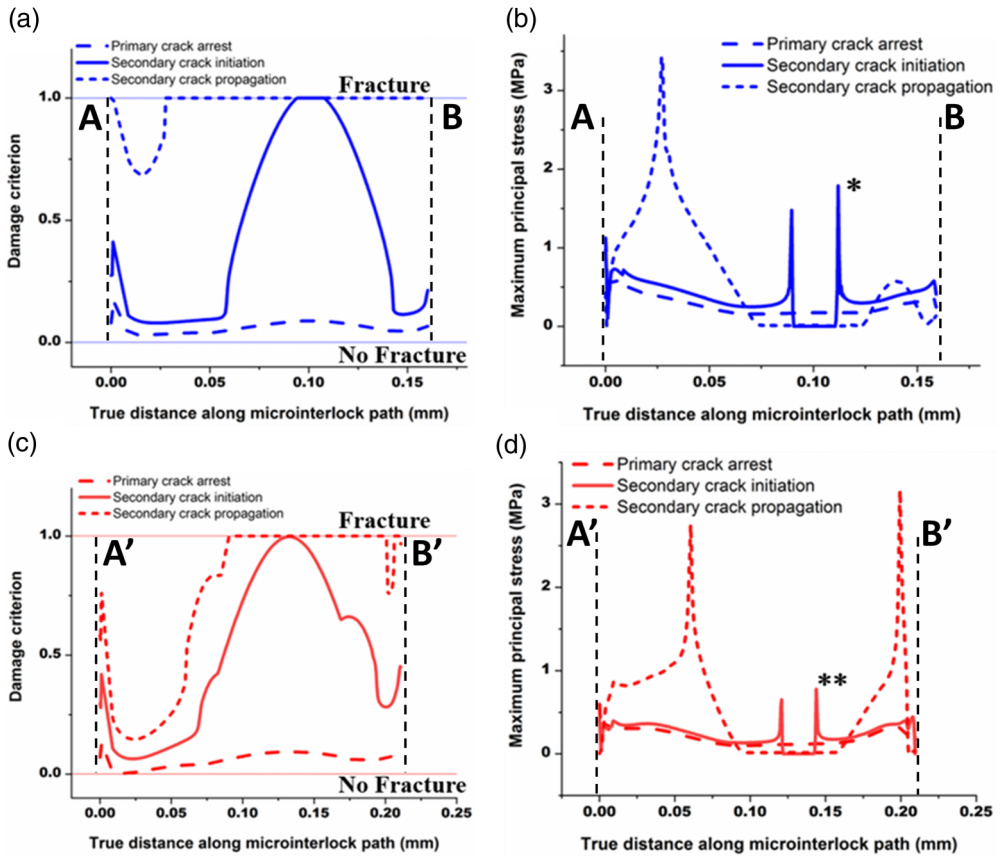

FIG. 7. Quantification of the primary crack arrest and secondary crack initiation events for the microinterlock fracture without and with the undercut. Point markers A and B and A′ and B′ depict the location of start and end points of the nonundercut and undercut microinterlock, respectively, as shown in Fig. 6. (a) Damage criterion (0 stands for no fracture and 1 stand for fracture) plotted against the true distance along the single nonundercut microinterlock path (with no precrack's path taken into consideration) for primary crack arrest, secondary crack initiation, and propagation. (b) Corresponding maximum principal stress in the case of the microinterlock fracture without undercut. The stress became zero when the secondary crack was initiated in both the cases that further propagated with two crack fronts. The asterisks marked the secondary crack initiation process as shown in Fig. 6. The conformity between the damage criterion and maximum principal stress indicated that the normal stress played a determining role in causing the fracture as compared to the shear stress. (c) Damage criterion plotted against the true distance along the single microinterlock path with the undercut. (d) Corresponding maximum principal stress plotted against the true distance along the single microinterlock with the undercut. Similar behavior was noted, however, with considerably less fracture propagation as a result of the undercut-based strain energy absorption.

fracture behavior by controlling the strain energy dissipation rates through crack arrests. The height of the singularity peaks indicated irreversible energy dissipation at the crack tips. A significant difference (≈4-fold) in the singularity peak heights was recorded between the undercut and nonundercut microinterlock's secondary fracture. This difference illustrated the role of undercut in the microinterlock's fracture that reduced the energy release rate available to the crack fronts and, consequently, conserved irreversible loss of strain energy. To determine the strain energy dissipation rate between the two different microinterlock geometries, the line integral of the difference in the area under the curves was calculated and divided by the total time step to obtain the energy rates. The comparison revealed a 23% decrease in the strain energy dissipation rate for the microinterlock with the undercut as compared to its nonundercut counterpart [Fig. 8(c)]. This increase in crack propagation inhibiting energy expenditure as a result of microscopic contact mechanics possibly explains why a propagating crack tends to move away from the biological micro-interlocked interfaces choosing another path with less resistance in the bulk [6,35].

In realistic fracture scenarios, the process would be considered dependent on friction; therefore we performed the above energetics study simulation with friction. The tangential contact interaction among the interacting parts with a friction coefficient of 1.63 was chosen based on the study conducted by Penkiy *et al.* [37]. The results, as shown in Fig. 19 in Appendix I for the single microinterlock fracture, suggested that the role of friction was significantly higher, which was ∼5-fold higher compared to the frictionless conditions. This result can be explained by the fact that friction greatly modified the shear or tangential interaction between the contacts as well as induced more strains or deformations in the model whose energy ultimately got dissipated via crack tips with higher energy release rates as compared with the frictionless condition. Finally, an external work versus strain energy comparison was made, as seen in Fig. 8(d). External work done was estimated by multiplying the force with the

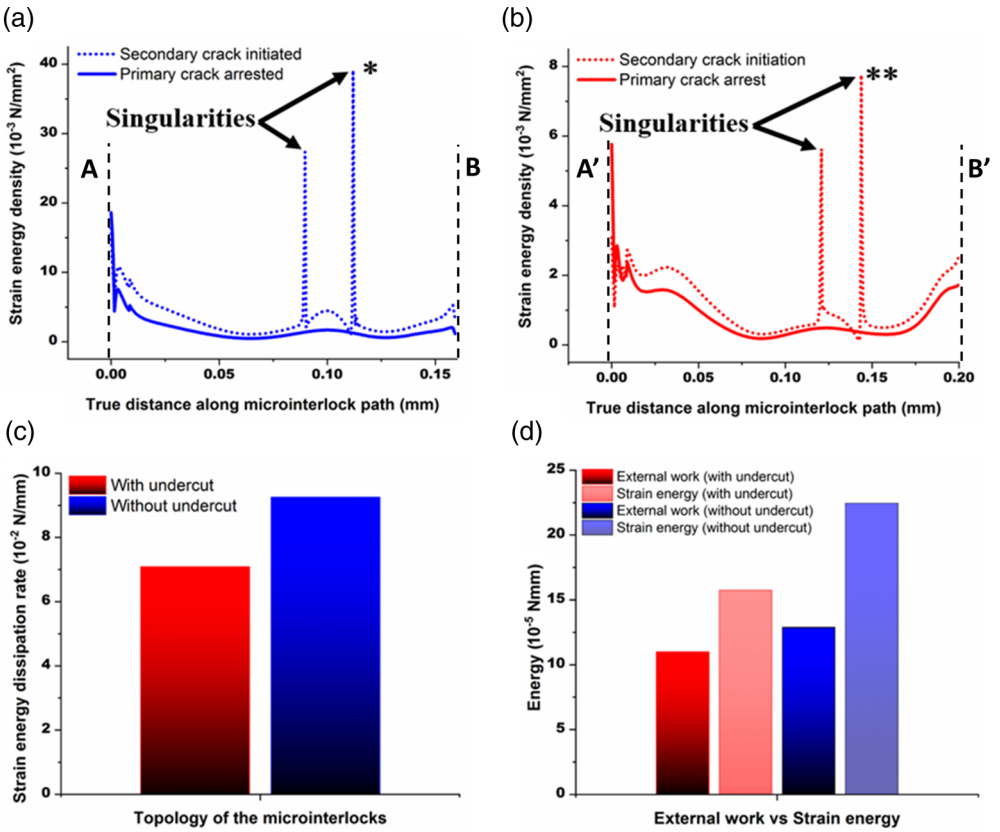

FIG. 8. Evaluation of strain energy density and dissipation rate for single microinterlock fracture with and without undercut. Point markers A and B and A′ and B′ depict location of start and end points of the nonundercut and undercut microinterlock, respectively, as shown in Fig. 6. (a) Comparison of strain energy density between the events of primary crack arrest and secondary crack initiation for the single microinterlock fracture without undercut. (b) Comparison of strain energy density between the events of primary crack arrest and secondary crack initiation for the single microinterlock fracture with the undercut. The peaks depicted singularities caused due to the maximum principal stress-energy dissipation via secondary crack fronts. The asterisks marked the respective secondary crack initiation events as shown in Fig. 6. The difference in the area under the interevent curves indicated the value of total strain energy dissipated during the events that can be calculated using line integral. (c) Comparison of strain energy dissipation between undercut and nonundercut. A decrease of 23% in the strain energy dissipation was observed for the undercut-based microinterlock as the undercut augmented the form-based interlocking via straining the region to a higher degree and not letting the energy dissipate via the crack tips. (d) Comparison between external work done and strain energy absorbed in the system for the whole model.

distance by which the interface was separated. In terms of the whole model, a ≈27% decrease in the external work for the undercut microinterlock as compared to the nonundercut microinterlock was recorded. This decrease was most likely due to reduced vertical movement (as external work is the product of applied external force and vertical displacement of the point of application) of the upper layer because of the undercut-based micromechanical interlocking effect. Also, a difference of ≈31% and ≈45% was noted between external work and strain energy for with and without undercut, respectively. The lower difference of the undercut-based microinterlock depicted a higher degree of strain in the bulk of the system as opposed to the crack propagation-based interfacial separation for relaxation. The above results indicated that the microinterlocks, especially with undercuts, increased the interfacial toughness, in which the externally applied work was absorbed by non-mode I straining and opening, hence leading to mode mixity and nonequilibrium channeling of strain energies as compared to the plain interface in response to catering the externally applied energies. As these contact-based crack arrest phenomena were not observed during the plain interface fracture, no comparison was made between the plain and microinterlocked interfaces in terms of energy expenditure. However, considering the catastrophic crack propagation observed during the plain interface fracture (both simulation and experimental), a significantly higher energy dissipation rate is most likely expected for the plain interface as compared to the microinterlocked interface.

VI. DISCUSSION

Fascinated by human skin dermal-epidermal microinterlocks, we aimed to study microinterlocked adhesive fracture in a soft material to determine the guiding mechanism behind the increased fracture toughness and strength of the microinterlocked interface. From experimental peel tests, we found interesting results among different topologies of the interface. In general, a significant increase in adhesion strength was found between the microinterlocked and the plain interface. When the density of the interlocks was increased by 5-fold,

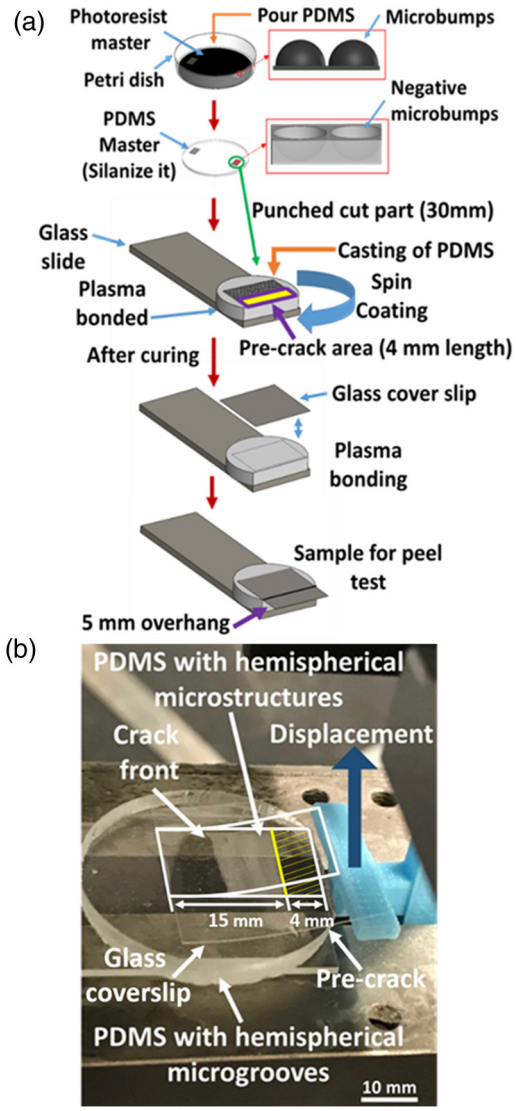

FIG. 9. Schematic of sample preparation and experimental setup. (a) Microstructures with or without undercut were fabricated using soft lithography and thermal reflow technique using silicon wafer and photoresist (AZ-40 XT). PDMS was poured, cured, replicated, and punched cut (30 mm diameter), which was plasma bonded to a glass slide. A precrack area having a length of 4 mm was added (highlighted in yellow). After plasma bonding, the PDMS layer with microgrooves (the negative of microbumps) was silanized using trichlorosilane. Then the area surrounding the microbump patch was covered by Scotch tape so the relevant area should be spin coated by PDMS only. After isolating the relevant area, PDMS was poured against the exposed silanized bottom PDMS layer, which was spin coated (750 rpm for 2 minutes). The tapes were removed as soon as the spin coating was finished. The thin spin-coated layer was cured and, finally, plasma bonded to a thin (170 μm) glass coverslip ($24\times24\,\mathrm{mm}^2$) with an overhang of 5 mm for peeling. (b) Experimental setup where the plasma-bonded glass coverslip was peeled off using a deflector mounted on an Instron universal testing machine. The reaction force during the peeling was recorded by a 50 N load cell fixed on the movable crosshead of the Instron® universal testing machine.

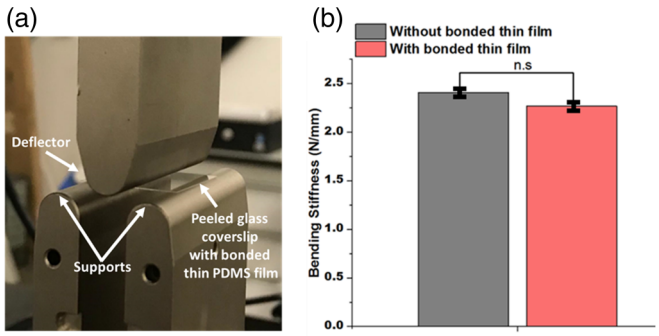

FIG. 10. Three-point bending experimental setup and results. (a) Three-point setup showing the deflector with a curved edge for pint contact and supports. The peeled layer consisted of a glass coverslip ($\approx$170 μm thick) plasma bonded with a thin PDMS layer ($\approx$100 μm thick). The force-displacement relationship was measured for the above configuration with and without bonded thin film for comparison. (b) The bending stiffness of the plate was determined from the slope of the linear region of the force-displacement curve. No significant difference was found between the glass coverslips with a plasma-bonded thin PDMS film and without it based on the t test. The total number of samples for each type of glass coverslips used was 10. The error plots show the standard deviation. The result implied that the bending characteristics of the peeling layer were not significantly affected by the plasma-bonded thin PDMS film if only small deflections were considered.

a significant increase in the damage initiation force was observed ($\approx$2-fold). We found a striking similarity between our results and those of Chung *et al.*, in which they attributed the increase in fracture toughness of the crosswise incised PDMS interface to the Cook-Gordon (C-G) mechanism. Their version of the C-G mechanism was 2D and ours 3D due to microinterlocks; therefore for comparison, we performed peel tests on plain strain patterned microinterlocks of the same dimension and horizontal spacing. We found that there was a significant decrease in damage initiation force between microinterlocks and plain strain patterns. To study the C-G mechanism-related events at a single microinterlock level, we performed a physics-based cohesive zone model, in which we found events like primary crack arrest and secondary crack initiation as a result of contact interactions. Between these events, a significant amount of energy was retained in the system as a result of microinterlock that would have dissipated via crack tips under plain conditions. The above-mentioned findings from our cohesive zone model confirm that the C-G mechanism guided and determined the peeling response under different topologically microinterlocked conditions. For example, in the plane strain patterns, no C-G mechanism was available widthwise as there were no microinterlocks to arrest the damage propagation. Thus a significant decrease in damage initiation force was observed. However, in the graph for plane strain patterns, significant hindrance towards fracture propagation after the damage initiation was seen as a result of C-G mechanism-induced crack arrest during lengthwise fracture propagation. It should be noted here that in our case, as seen from the cohesive zone model output, the

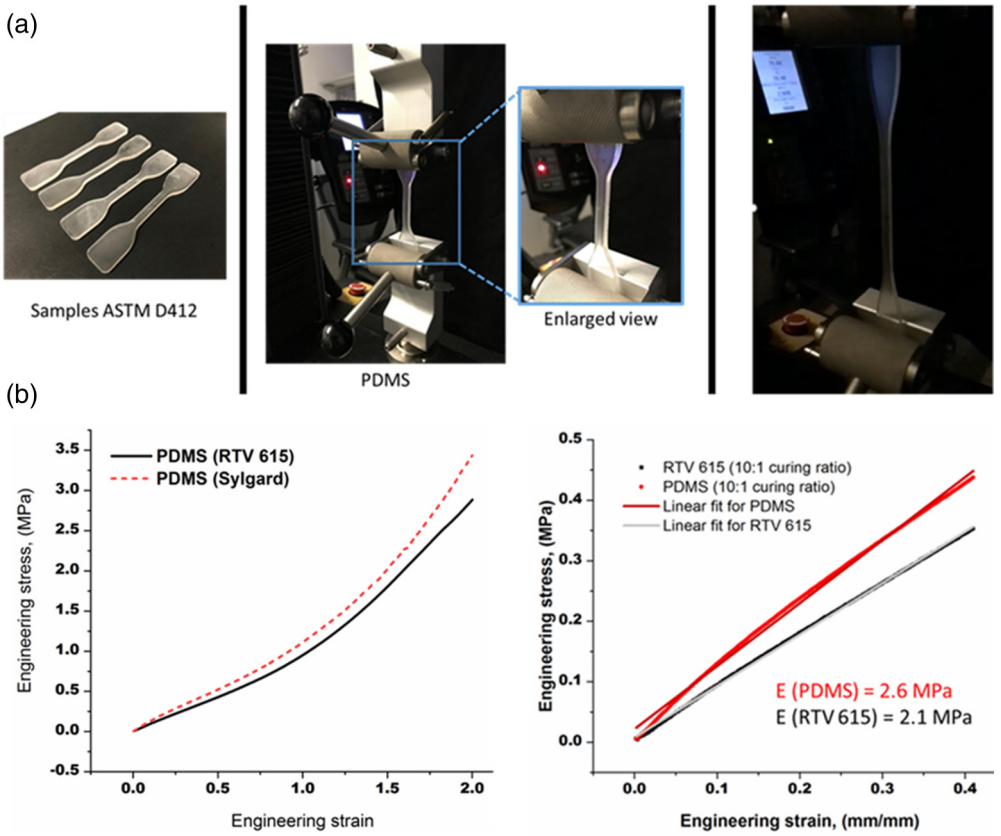

FIG. 11. Experimental uniaxial tensile characterization of PDMS. (a) ASTM D412 was used as a standard to characterize PDMS (Sylgard 184 and RTV 615). The strain rate of 5 mm/s was used for deformation. (b) Engineering stress versus strain response for different Sylgard 184 and RTV 615. 40% strain was used to capture the linear response and to calculate Young's modulus of elasticity.

primary crack and secondary crack were in different planes as opposed to other research studies done in composites vis-à-vis the C-G mechanism [23–25].

The outcome of this study highlighted the role of soft microinterlocks in creating sturdy interfaces that can maintain their functionality in mechanically unstable environments (like *in vivo*). Our findings of contact-based stress transmission of these microinterlocks lay foundations for a rational design of electronic skin (e-skin) and prosthetics as well as soft robotics [11,12,20]. For example, to rationally decide where to place mechanical sensors for highly sensitive tactile sensing in e-skin, our FEM suggests the vicinal region near the secondary crack initiation as an ideal site to place sensors for highest pressure sensitivity to external mechanical stimuli in analogy to nociceptors in the skin. We also foresee potential applications of this study in the field of 3D bioprinting, where adherence between the printed layers plays a crucial role in determining mechanical integrity and stackability as well as shape fidelity of printed scaffolds or tissue layers [50–53]. It can also be prominently applied in the field of sutureless skin graft applications as biosealants along with a platform for drug delivery [54]. Last but not the least, the viscoelastic energy dissipation of the microinterlocks can be further explored to create bioinspired tough adhesives that can function under wet conditions [21,26,49].

Regarding limitations, the 2D idealization of the hemispherical microinterlock did not represent the actual geometry, which in actuality was 3D. Therefore, it would not be possible to accurately explain the fully peeled experimental results quantitatively in via a 2D simulation model, but 3D simulations are exorbitantly computationally expensive to attain that. Keeping this in mind, we aimed to critically visualize the single microinterlock fracture and associated crack propagation to find the determining mechanism that augmented the experimental fracture toughness. Using a combined approach of the experimental study on various microinterlocked topologies and a physics-based cohesive zone model, we were able to identify primary crack arrest and secondary crack initiation at the single microinterlock level that provided evidence for the C-G mechanism to be the determining mechanism for fracture toughness augmentation. Even though limited in scope, our approach still could give an insight into the highly nonlinear nature of the process and interpret the microinterlock's fracture guiding mechanism such as the C-G mechanism, which otherwise is highly cumbersome to be interpreted experimentally. These findings can help us in highlighting the underlying fracture mechanism that decides the interfacial toughness and rational design of a robust soft interface for various technical applications.

VII. CONCLUSION

A fully physics-based FEM was developed to visualize the single microinterlock fracture between two soft PDMS

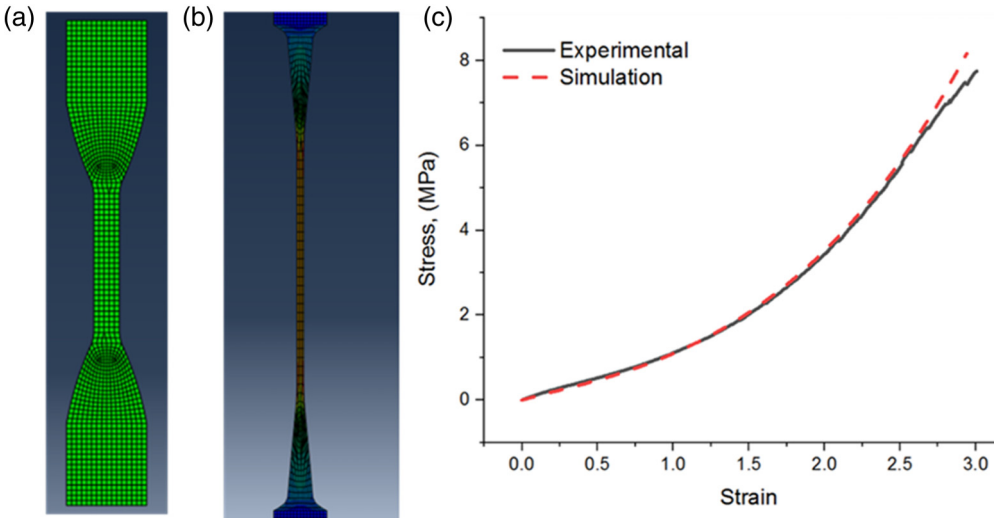

FIG. 12. Virtual 2D plane strain tensile test to validate Ogden fit (mu1 = 0.291, alpha1 = 5.215, D1 = 0) hyperelastic behavior of PDMS. (a) Mesh global size of 0.75 was used for the simulation and geometry was taken from the ASTM D412 standard. (b) Uniaxially deformed specimen with amplified stress in the test region. (c) Stress versus strain curve for experimental and simulation. A close fit was achieved between the two indicating that the Ogden fit parameters captured the material behavior of PDMS in the hyperelastic regime.

layers. The study revealed contact interaction-based phenomena where the primary propagating crack was arrested and the secondary crack was initiated in the microinterlocked area.

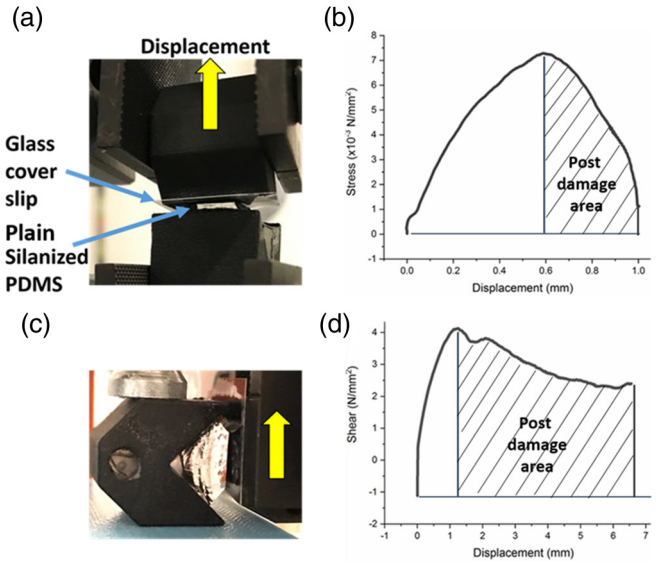

FIG. 13. Experimental setup to determine the damage initiation criteria. (a) Normal-only fracture test. (b) The graph between stress and displacement shows rampant fracture behavior where the interface is separated by 1 mm displacement. (c) Shear-only fracture test. (d) The graph between stress and displacement shows slow and delayed fracture behavior due to the sliding-based shear interaction where the interface did not separate even after 7 mm of displacement. The analysis showed that the normal only mode was highly vulnerable towards interfacial fracture, hence the maxima of the graph as well slope of the prefractured region were chosen as the starting values to model fracture initiation of the plain interface for the cohesive zone simulation. For the mode-mixity consideration area under the curve postfracture for normal only (0.00024 N/mm) and shear only (0.235 N/mm) were considered.

Between these events, the strain energy remained stored in the system that would have otherwise been dissipated irreversibly via crack tips. Strain energy analysis confirmed the significantly lower strain energy dissipation rate for the microinterlock with the undercut as compared to its nonundercut counterpart. These phenomena were completely absent in plain interface fracture where a fracture propagated catastrophically without any arrests. The Cook-Gordon mechanism as the underlying fracture toughening mechanism of the primary crack arrest and the secondary crack initiation elucidated the difference in the mechanically obtained experimental results for different interfacial topologies. The outcomes of this study allow a deeper understanding of the microscale interlocking interface between soft layers and its fracture behavior. They could prominently help in rationally deciding location sites of pressure sensors for highly sensitive tactile sensing in e-skin applications. Our FEM study could also help us to understand why certain vital mechanical receptors of the human skin are preferably found in specific locations of the dermal layer which might be the zones of the highest mechanical stress generated under shear force as a result of dermal-epidermal microinterlock interaction. Further implications of our study are expected in the field of 3D bioprinting, sutureless skin graft, soft robotics, prosthetics, and biological adhesives.

ACKNOWLEDGMENTS

We thank the NYU Abu Dhabi graduate office for providing N.S.B. the NYU Abu Dhabi Global Ph.D. Fellowship. We also thank NYU Abu Dhabi Core Technology Platform for providing us access to SEM, NYUAD microfabrication core facility clean room, and 3D printer. We acknowledge the annual research grant provided by NYU Abu Dhabi. We acknowledge Jongmin Kim's support in performing the contact angle experiment.

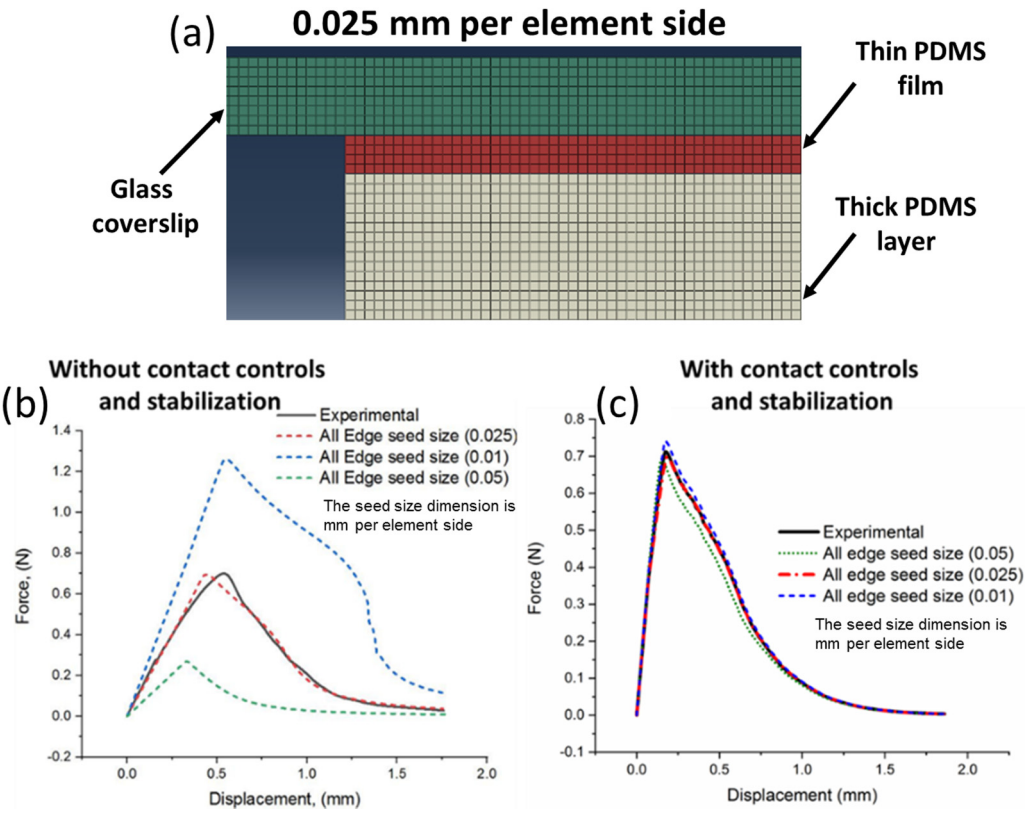

FIG. 14. Effect of the mesh size on the force versus displacement response without and with contact control and stabilization. (a) Meshed model and assembly with all edge seed size of 0.025 mm per element side for all parts. (b) The force-displacement response showed a highly sensitive response towards mesh refinement due to the path-dependent nature of the slave node fracture criterion that was associated with the cohesive surface interaction between the parts when contact stabilization was not incorporated in the interaction property manager. With the experimentally obtained fracture parameters, a mesh size with all edge size of 0.025 mm per element side led to the best fit among tested mesh sizes in terms. Due to this conundrum, a mesh convergence study was not possible. However, when contact controls were incorporated with automatic stabilization this problem was no longer there and mesh convergence was established as can be seen in (c). Keeping in view the enormous difference in computational time (100 times higher) between the seed size 0.025 mm per element side and 0.01 mm per element side as well as the low deviation in the difference of their results the seed size of 0.025 mm per element side was chosen for the analysis.

APPENDIX A: FABRICATION AND EXPERIMENTAL SETUP

We fabricated a 2D array of hemispherical microstructures of $\approx 50\,\mu$m in diameter on a patch area of $15\times 20\,\text{mm}^2$ with an undercut up to $\approx 20^\circ$ in PDMS ($n = \approx$ 60 000 and $n = \approx$ 12 000). First, an array of 40 μm$\times$40 μm pedestals with a height of 5 μm was etched on a silicon wafer with the deep reactive ion etching method. After patterning AZ 40XT, a positive photoresist, on top of the pedestals, the wafer was thermally reflown on a hotplate at 120 °C for 60 sec to generate microstructures with an undercut. The PDMS was cast and replicated from the master, which was further silanized using Trichloro (1H, 1H, 2H, 2H, perfluoro) octylsilane as shown schematically in Fig. 9(a). For fracture test sample preparation, a circular PDMS patch with a diameter of 30 mm was punched out from the PDMS master and plasma-bonded unto the glass slide. Then the area surrounding the microbump patch was covered by Scotch tape so that the relevant area should be spin coated by PDMS only. After isolating the relevant microbump area, 0.5 g of PDMS mixed with a curing agent (10:1 ratio) was poured against the exposed silanized bottom PDMS layer, which was spin coated (750 rpm for 2 min). The tapes were removed as soon as the spin coating was finished. After curing the spin-coated layer, a glass coverslip ($24\times 24\,\text{mm}^2$ and 170 μm thick) was plasma bonded with an overhang of 5 mm for the single cantilever bending peel test under controlled displacement at a displacement rate of 5 μm/s. The force-displacement results were recorded with 50 N load cell for plain and hemispherical microinterlocks without and with an undercut. An extra 4 mm length was given for precrack consideration near the microinterlocked patch area during the peeling experiments, as shown in Fig. 9(b). Care was taken to introduce a precrack in the interface by prepeeling the interface starting from the cut edge till the microinterlocked patch's end using the Instron machine's setup. Once the precrack line met the edge line of the microinterlocked patch areas' end, the force-displacement readings were recorded.

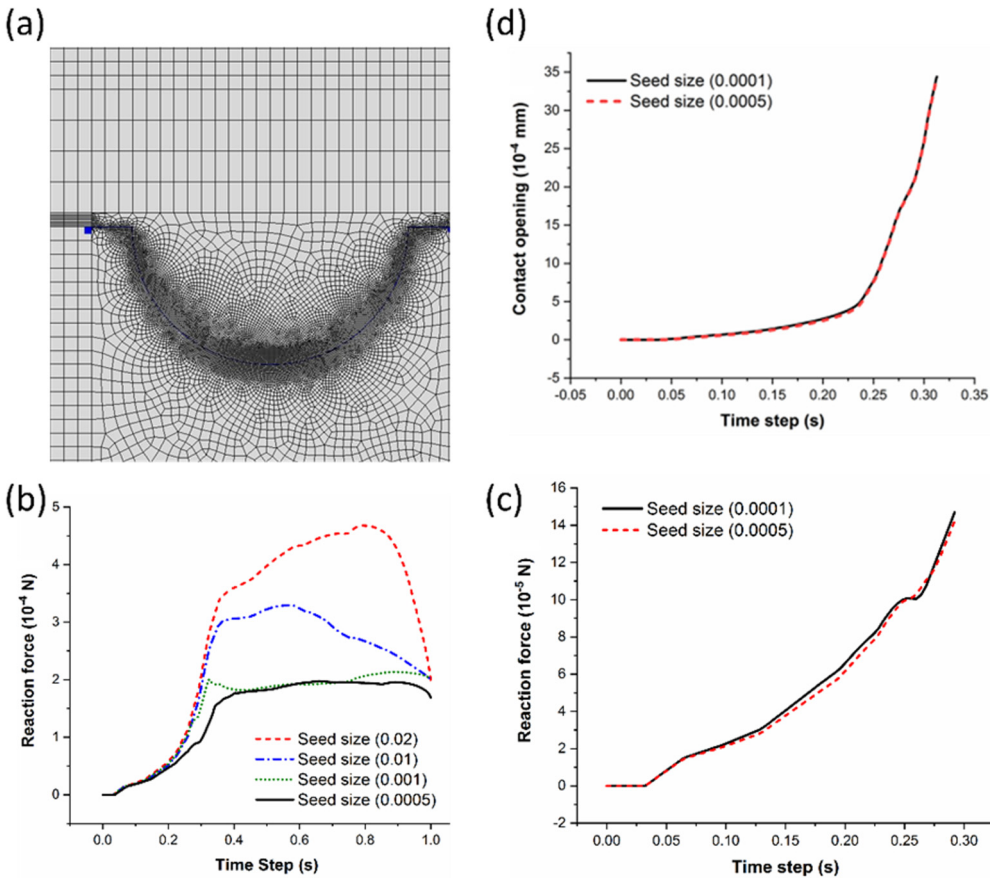

FIG. 15. The meshed model of seed interface size 0.0005 mm per element side on the contact interface and mesh convergence study. (a) The interface was finely meshed (seed size of 0.0005 mm per element side on the contact interface) to avoid any computational artifacts that could possibly affect the fracture results. A submodeling routine was used to translate the boundary conditions from the related global model, which enabled us to reduce the computational time significantly as well as to compare the different microinterlock topologies for a given time step. (b) The mesh convergence study showed that the mesh converged near the interface seed size of 0.0005 mm per element side on the contact interface, and for the seed size below that, the computational time significantly increased with very little difference in the results. For example, for the seed size of 0.0001 mm per element side on the contact interface, as seen in (c), the computational time increased 100 times with significantly less difference in the output. Therefore the interface seed size of 0.0005 mm per element side on the contact interface was chosen for the analysis. (d) No significant difference in contact opening was observed for the seed size of 0.0005 mm per element side and the seed size of 0.0001 mm per element side.

APPENDIX B: CHARACTERISTIC STRESS DECAY LENGTH

In our experiment, the peeling layer consisted of a flexible glass coverslip ($\approx$170 μm thick) plasma bonded with a thin PDMS layer ($\approx$100 μm), which was different from the previous studies as mentioned in the main text. In their studies, the peel layer consisted of a glass coverslip without a bonded thin film. To verify whether these two plates were comparable, we conducted a three-point bending experiment first, as shown in Fig. 10. The experiment confirmed that the bending behavior remained essentially the same even after bonding a thin PDMS sheet to the bare thin and flexible glass coverslip. We made use of the slope of the obtained force-displacement curve and equated it to the slope of the classic beam equation. When dividing the result by the width of the plate, we obtained a flexural rigidity of 0.029 Nm in close agreement with 0.031 Nm for the flexural rigidity of plates from $[\frac{Et^3}{12(1-\upsilon^2)}]$, where E is Young's modulus of elasticity of the plate, t is the thickness of the plate, and υ is the Poisson's ratio.

APPENDIX C: MATERIAL MODELING

As the curing temperature and time change the properties of PDMS significantly, we evaluated the material properties of the PDMS from Sylgard at the commonly used 1:10 curing ratio that was cured at 70 °C for 30 min.

1. Material properties for the elastic bottom layer

Due to the relatively large thickness of the bottom layer at 5 mm, we assumed it was a continuum elastic deformable body. The Young's modulus of elasticity was estimated using an ASTM D412 uniaxial tensile engineering stress-strain response [Fig. 11(a)]. Two types of PDMS (Sylgard 184 and RTV 615) were used for the test, which was strained up to 200% [Fig. 11(b)]; however, the initial 40% of strained

behavior was linearly fitted to obtain the slopes. A factor of 0.5 was used as the conversion factor to take care of the difference between engineering and true stress-strain behavior. The obtained values of modulus for Sylgard 184 and RTV 615 were 2.6 MPa and 2.1 MPa, respectively. The Poisson's ratio of 0.45 was used considering the incompressible nature of PDMS and convergence of the FEM.

2. Material properties for the hyperelastic top layer

The 100 μm thin top layer was hyperelastic, and, therefore, elastic material properties could not capture its physical response. Therefore, hyperelastic material fit parameters were needed to model the behavior for which the Ogden hyperelastic model was used [4]. Ogden fit material parameters were obtained via curve fitting the uniaxial engineering stress-strain response. The curve fitting was performed using the material evaluation module in Abaqus Standard. The evaluation revealed a stable fit up to 300% strain. The obtained Ogden material parameters were mu1 = 0.291, alpha1 = 5.215, and D1 = 0.

3. Uniaxial hyperelastic response test

To check the hyperelastic uniaxial response using the obtained Ogden parameters, a virtual tensile test was conducted with Abaqus Standard. The geometry of the specimen was kept the same as experimental (ASTM D412) and a 2D plane strain approximation was used to model the stress-strain behavior. The elements used for the simulation were four-node bilinear plane strain quadrilateral, hybrid, and constant pressure. For the mesh size, the approximate global size of 0.75 was used with curvature control [Fig. 12(a)]. The bottom edge was fixed in all degree of freedoms, and the top edge was displaced longitudinally by 300% strain [Fig. 12(b)]. The experimental and simulation stress-strain response closely matched each other [Fig. 12(c)], indicating that the material response was effectively captured by the obtained Ogden fit parameters. The mesh convergence study revealed no effect of mesh density on the stress-strain response output.

APPENDIX D: DAMAGE CRITERION AND MODE MIXITY

The interfacial fracture behavior was modeled using surface-based cohesive interaction in which traction separation-based damage initiation and evolution parameters determined the degradation and eventual failure of the bond between two contact surfaces. The process of failure was initiated when the contact surfaces satisfied the provided stress or separation-based criterion. We chose the maximum nominal stress-based criterion to model the fracture with the Benzeggah-Kenane (BK) criterion for mode mixity. To determine which mode was more vulnerable towards fracture, normal-only mode and shear-only mode fracture experiments were carried out with custom-made samples, which were designed following the specifications of the peel test samples, as shown in Fig. 13. As per the response obtained, the normal-only mode was highly vulnerable towards damage as the displacement at the maximum ($\approx$0.6 mm) was significantly higher than the shear-only displacement at the maximum ($\approx$1 mm). Also, the shear mode subsequent damage evolution was significantly slower than the normal-only mode. Hence the normal-mode fracture behavior was considered to model fracture behavior. The linear fit slope of the predamage region (0.025 N/mm) of the normal only response was used as the initial guess for the uncoupled cohesive penalty stiffness coefficients and the maxima (0.0075 N/mm^2) of the normal-only response as the damage initiation criterion in the Abaqus interaction property manager. The same above-mentioned cohesive properties were used for normal and shear directions to reduce the total number of unknowns. For the mode-mixity consideration area under the curve postfracture for normal only (0.00024 N/mm) and shear only (0.235 N/mm) were considered.

APPENDIX E: MESH CONVERGENCE STUDY

First, the simulations were run without contact controls and automatic stabilization using the interaction manager. As a result, it was found that the output was highly sensitive towards mesh refinement as can be seen in Fig. 14(a); hence, mesh convergence was not possible to achieve. To solve this problem, the model's contact interaction was automatically stabilized by using contact controls in the interaction property manager. Consequently, accurate mesh convergence was attained with the refinement of mesh size, as seen in Fig. 14(b). The total number of elements for seed sizes 0.05 mm per element side, 0.025 mm per element side, and 0.01 mm per

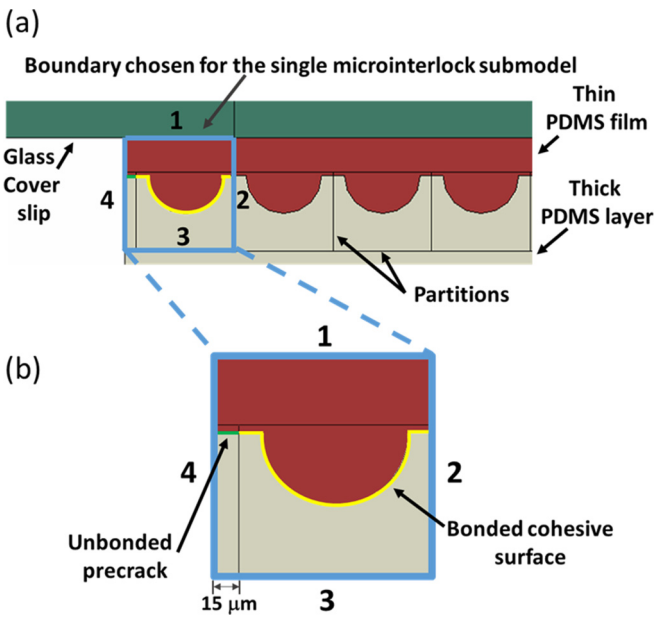

FIG. 16. Partitioning, submodel, and boundary condition transfer from the global model. (a) Schematic showing the microinterlocked assembly and the partitioning done in the global model starting from the edge till 15 μm for the precrack and then at regular intervals of 130 μm till the end of the contact line of the interface. The horizontal partitioning was done 100 μm below the contact line. The boundary for the single microinterlock submodel is numbered 1, 2, 3, and 4. (b) Enlarged view of a single microinterlock submodel that has been generated after removing all other faces keeping only the concerned region. To run the submodel the boundary conditions from the global model were transferred to boundaries 1, 2, 3, and 4, respectively, in the submodel.

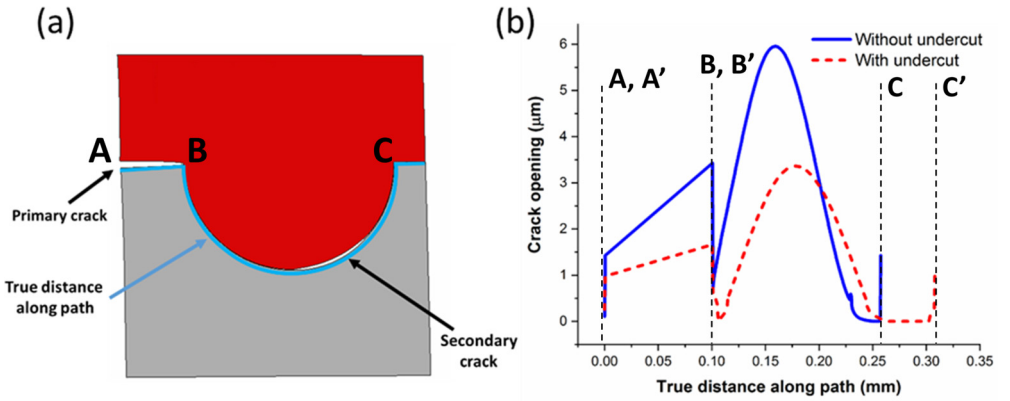

FIG. 17. Crack opening as a function of true distance along the microinterlocked path for the same time step of the simulation. (a) Deformed microinterlock at the secondary crack initiation stage showing the true distance along the path. The amount of crack opening was calculated for a single microinterlock without and with the undercut. Point markers A, B, C and A′, B′, C′ depict location of point markers along the line and around the semicircular path for the nonundercut and undercut microinterlock, respectively. (b) Crack opening versus true distance along the path. As expected, a significantly lower crack opening was obtained for the microinterlock with the undercut as compared to its nonundercut counterpart.

element side considering the whole assembly of the parts were 32 200, 1 86 400, and 8 05 000. The seed size of 0.025 mm per element side was chosen keeping in view the small difference in the output as compared to the 0.01 mm per element side seed size; however, on the other hand, the computational time became exorbitantly increased 100 times as a result of the 4-fold increase in the number of elements. To determine the effect contact controls and automatic stabilization on the model's solution accuracy, energy comparison between the total strain energy and the sum of all viscous damping and stabilization energies was performed. As per the results, the amount of energy inserted in the system for the contact controls in the form of stabilization energy was significantly less (less than 1%) as compared to the total strain energy of the system and hence did not affect the model's solution significantly. Figure 15 shows the meshed model of seed interface size of 0.0005 mm per element side on the contact interface as well as the associated mesh convergence study results.

APPENDIX F: SUBMODELING

The microinterlocked model was rerun but with partitions concerning the boundary edges of the relevant microinterlocks as shown in Fig. 16(a). Keeping the partitioned face of the first microinterlock in the assembly space and removing the rest of all other faces, the model was changed to submodel type, as seen in Fig. 16(b). Under the edit attributes section, the submodel was then made to read results from the global model by typing the exact name of the global model's output

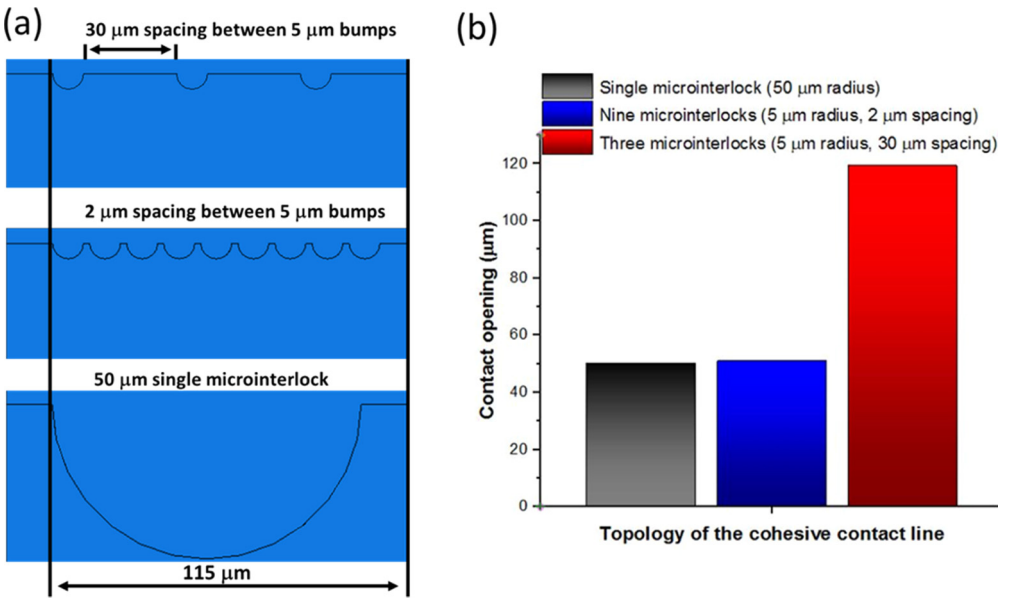

FIG. 18. Contact opening comparison for different surface topologies at the same cohesive contact line length of 115 μm. (a) Schematic showing comparison between three, nine and one interlock of different length scales and interspacing. (b) Contact opening comparison results obtained from a single microinterlock model for different scale and density of microbumps.

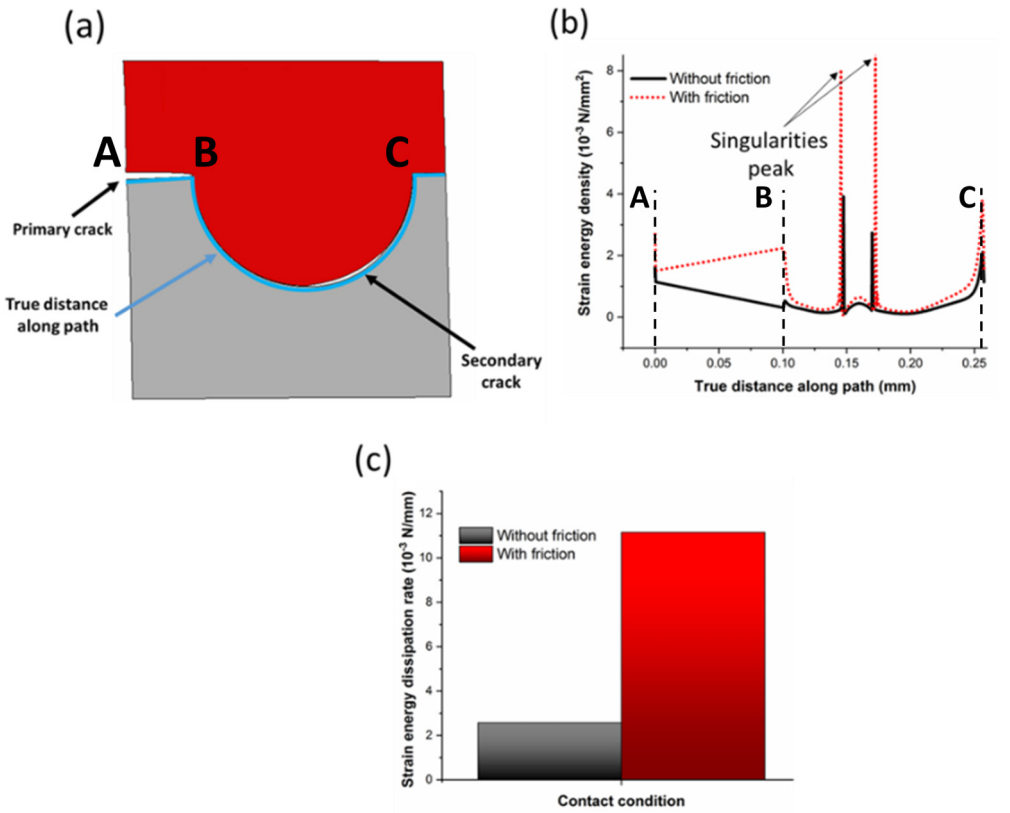

FIG. 19. Strain energy dissipation rate with and without friction for single microinterlock fracture. (a) Deformed microinterlock at the secondary crack initiation stage showing the true distance along the path where the crack opening was calculated for friction and nonfriction cases. Point markers A, B, C depict location of point markers along the line and around the semicircular path for the microinterlock. (b) Strain energy density plotted against true distance along the path for both the cases. (c) Strain energy dissipation rate as obtained via line integral and compared for both cases.

file. Next, the relevant boundaries of the partitioned assembly were chosen, and boundary conditions that were generated during the job execution of the global model were translated to the submodel. In this way, exact translation and rotational degrees of freedoms were given to the single microinterlock partitioned boundaries to let them undergo fracture in the same way it would have been undergoing in the global model. Hence, based on the results from the global model, submodeling of the single microinterlock fracture was performed but with refined mesh and less computational time.

APPENDIX G: CONTACT OPENING COMPARISON

Crack opening comparison between undercut and nonundercut microinterlocks as a function of true distance along the path is shown in Fig. 17.

APPENDIX H: SIZE AND DENSITY COMPARISON

Contact opening comparison for different surface topologies at the same cohesive contact line length of 115 μm was done using the single microinterlock model, as seen in Fig. 18(a). The contact and boundary conditions were kept the same for all cases. The results, as seen in Fig. 18(b), suggested that highly dense 5 μm (radius) microinterlocks produced similar effects in terms of contact opening as compared to one 50 μm (radius) microinterlock. However, widely spaced 5 μm (radius) interlocks showed a significant increase in contact opening as compared to the other two microinterlocks. Therefore, based on the simulation data, smaller and denser microinterlocks can alter the surface fracture properties significantly via controlling the contact opening through microinterlocking energy dissipating mechanisms.

APPENDIX I: FRICTION

As per the simulation results performed with friction condition, a significantly higher strain energy dissipation rate difference was found between the pairs, which is ≈5-fold, as seen in Fig. 19. The results could be attributed to the significant contribution of friction concerning tangential or shear deformation during contact interaction.

[1] R. W. Murphree, Nurs. Clin. North Am. **52**, 405 (2017).

[2] A. Dehdashtian, T. P. Stringer, A. J. Warren, E. W. Mu, B. Amirlak, and L. Shahabi, in *Melanoma* (Springer, Cham, 2018), pp. 15–26.

[3] K. Wang, Z. Lou, L. Wang, L. Zhao, S. Zhao, D. Wang, W. Han, K. Jiang, and G. Shen, ACS Nano **13**, 9139 (2019).

[4] Y. Gilaberte, L. Prieto-Torres, I. Pastushenko, and Á. Juarranz, in *Nanoscience in Dermatology* (Academic Press, Cambridge, MA, 2016), pp. 1–14.

[5] X. Xiong, T. Wu, and S. He, Med. Hypotheses **81**, 883 (2013).

[6] J. W. Pro and F. Barthelat, MRS Bull. **44**, 46 (2019).

[7] A. J. Crosby, M. Hageman, and A. Duncan, Langmuir **21**, 11738 (2005).

[8] A. Ghatak, L. Mahadevan, J. Y. Chung, M. K. Chaudhury, and V. Shenoy, Proc. R. Soc. A **460**, 2725 (2004).

[9] T. Thomas and A. J. Crosby, J. Adhes. **82**, 311 (2006).

[10] F. Barthelat, Philos. Trans. R. Soc. A **365**, 2907 (2007).

[11] J. Park, Y. Lee, J. Hong, Y. Lee, M. Ha, Y. Jung, H. Lim, S. Y. Kim, and H. Ko, ACS Nano **8**, 12020 (2014).

[12] Y. Wu, Y. Liu, Y. Zhou, Q. Man, C. Hu, W. Asghar, F. Li, Z. Yu, J. Shang, G. Liu, M. Liao, and R. W. Li, Sci. Robot. **3**, eaat0429 (2018).

[13] L. Pu, R. Saraf, and V. Maheshwari, Sci. Rep. **7**, 5834 (2017).

[14] T. Wang, Y. Zhang, Q. Liu, W. Cheng, X. Wang, L. Pan, B. Xu, and H. Xu, Adv. Funct. Mater. **28**, 1705551 (2018).

[15] M. Mirkhalaf, A. K. Dastjerdi, and F. Barthelat, Nat. Commun. **5**, 3166 (2014).

[16] U. Yadav, M. Coldren, P. Bulusu, T. Sain, and S. Ghosh, Mech. Mater. **137**, 103107 (2019).

[17] W. S. Kim, I. H. Yun, J. J. Lee, and H. T. Jung, Int. J. Adhes. **30**, 408 (2010).

[18] E. D. Reedy, Jr., N. R. Moody, J. A. Zimmerman, X. Zhou, M. S. Kennedy, W. M. Mook, and D. F. Bahr, Effect of nanoscale patterned interfacial roughness on interfacial toughness, Technical Report Number(s): SAND2007-5990, TRN: US200803%%19 (Sandia National Laboratories, Albuquerque, New Mexico, USA, 2007).

[19] B. M. Z. Newby and M. K. Chaudhury, Langmuir **13**, 1805 (1997).

[20] M. Ha, S. Lim, S. Cho, Y. Lee, S. Na, C. Baig, and H. Ko, ACS Nano **12**, 3964 (2018).

[21] A. Majumder, A. Ghatak, and A. Sharma, Science **318**, 258 (2007).

[22] N. Chaudhari, T. Deshpande, Y. R. G. Singh, S. Patil, M. Kulkarni, J. Raut, and A. Sharma, Soft Matter **13**, 2394 (2017).

[23] J. Y. Chung and M. K. Chaudhury, J. R. Soc. Interface **2**, 55 (2005).

[24] M. Raab, E. Schulz, and M. Sova, Polym. Eng. Sci. **33**, 1438 (1993).

[25] J. C. Hill, S. J. Bennison, P. A. Klein, J. W. Foulk, A. Jagota, and S. Saigal, Int. J. Fract. **119**, 365 (2003).

[26] S. Patil, A. Malasi, A. Majumder, A. Ghatak, and A. Sharma, Langmuir **28**, 42 (2012).

[27] F. A. Cordisco, P. D. Zavattieri, L. G. Hector, and B. E. Carlson, Int. J. Solids Struct. **83**, 45 (2016).

[28] M. Alfano, S. Pini, G. Chiodo, M. Barberio, A. Pirondi, F. Furgiuele, and R. Groppetti, J. Adhes. **90**, 384 (2014).

[29] Y. Li, C. Ortiz, and M. C. Boyce, J. Mech. Phys. Solids **61**, 1144 (2013).

[30] C. Dong, C. Yuan, A. Xu, X. Bai, and Y. Tian, Langmuir **35**, 2878 (2019).

[31] M. Bazrafshan, M. B. de Rooij, and D. J. Schipper, Tribol. Int. **121**, 381 (2018).

[32] N. Maeda, N. Chen, M. Tirrell, and J. N. Israelachvili, Science **297**, 379 (2002).

[33] F. Barthelat, Int. Mater. Rev. **60**, 413 (2015).

[34] J. W. Pro and F. Barthelat, Acta Biomater. **94**, 536 (2019).

[35] F. Barthelat, Z. Yin, and M. J. Buehler, Nat. Rev. Mater. **1**, 16007 (2016).

[36] Abaqus Standard User's Manual, version 6.1, Dassault Systèmes Simulia Corp., Providence, RI (2016).

[37] I. Penskiy, A. P. Gerratt, and S. Bergbreiter, in *Proceedings of the 2011 IEEE 24th International Conference on Micro Electro Mechanical Systems* (IEEE, Piscataway, NJ, 2011), pp. 440–444.

[38] C. K. Desai, S. Basu, and V. Parameswaran, J. Adhes. **92**, 819 (2016).

[39] S. Rajan, M. A. Sutton, R. Fuerte, and A. Kidane, Eng. Fract. Mech. **187**, 404 (2018).

[40] A. K. Dastjerdi, M. Pagano, M. T. Kaartinen, M. D. McKee, and F. Barthelat, Acta Biomater. **8**, 3349 (2012).

[41] K. Ha, H. Baek, and K. Park, Appl. Math. Model. **39**, 5828 (2015).

[42] H. Yu, J. S. Olsen, V. Olden, A. Alvaro, J. He, and Z. Zhang, Eng. Fract. Mech. **166**, 23 (2016).

[43] Y. F. Gao and A. F. Bower, Model. Simul. Mater. Sci. Eng. **12**, 453 (2004).

[44] J. Ebadi-Rajoli, A. Akhavan-Safar, H. Hosseini-Toudeshky, and L. F. M. da Silva, Mech. Mater. **143**, 103322 (2020).

[45] K. Kendall, Science **263**, 1720 (1994).

[46] K. L. Johnson, K. Kendall, and A. D. Roberts, Proc. R. Soc. A **324**, 301 (1971).

[47] See Supplemental Material at http://link.aps.org/supplemental/10.1103/PhysRevE.102.012801 for Movie 1: The movie shows the primary crack arrest and secondary crack initiation phenomena for the single microinterlock fracture without undercut. The model runs till 0.54 s of time step. Movie 2: The movie shows the primary crack arrest and secondary crack initiation phenomena for the single microinterlock fracture with undercut. The model runs till 0.54 s of time step.

[48] J. Barés, D. Bonamy, and A. Rosso, Phys. Rev. E **100**, 023001 (2019).

[49] A. Ghatak and M. K. Chaudhury, Langmuir **19**, 2621 (2003).

[50] V. Mironov, T. Trusk, V. Kasyanov, S. Little, R. Swaja, and R. Markwald, Biofabrication **1**, 022001 (2009).

[51] H. M. Powell and S. T. Boyce, Biomaterials **27**, 5821 (2006).

[52] H. Yoon, J. S. Lee, H. Yim, G. Kim, and W. Chun, RSC Adv. **6**, 21439 (2016).

[53] Y. J. Seol, J. Y. Park, W. Jeong, T. H. Kim, S. Y. Kim, and D. W. Cho, J. Biomed. Mater. Res. A **103**, 1404 (2015).

[54] S. Y. Yang, E. D. O'Cearbhaill, G. C. Sisk, K. M. Park, W. K. Cho, M. Villiger, B. E. Bouma, B. Pomahac, and J. M. Karp, Nat. Commun. **4**, 1702 (2013).